SEDIMENTOLOGY the journal of the International Association of Sedimentologists IAS

Sedimentology (2024) **71**, 2358–2377 doi: 10.1111/sed.13218

Siderite from the Tibetan Himalaya: Evidence for a low sulphate ocean during Oceanic Anoxic Event 1a (Early Aptian)

FAN MENG*, ZHONG HAN*,† , XIUMIAN HU† , HUGH C. JENKYNS‡ , BOLIN ZHANG*, XI CHEN§ and MINGCAI HOU*

**State Key Laboratory of Oil and Gas Reservoir Geology and Exploitation and Key Laboratory of Deep-Time Geography and Environment Reconstruction and Applications, MNR, Institute of Sedimentary Geology, Chengdu University of Technology, Chengdu 610059, China (E-mail: hanzhong19@cdut.edu.cn)*

†State Key Laboratory of Mineral Deposit Research, School of Earth Sciences and Engineering, Nanjing University, Nanjing 210023, China

‡Department of Earth Sciences, University of Oxford, South Parks Road, Oxford OX1 3AN, UK

§State Key Laboratory of Biogeology and Environmental Geology, China University of Geosciences, Beijing 100083, China

Associate Editor – Ying Zhou

ABSTRACT

Mesozoic oceanic anoxic events were characterized by relatively low seawater sulphate concentrations ($[SO_4^{2-}]$), which likely regulated the development and evolution of these major palaeoceanographic phenomena. However, there is little reliable sedimentary evidence for low $[SO_4^{2-}]$ in ancient marine waters and understanding of how such a seawater chemistry potentially impacted oceanic anoxic events is limited. This study presents an integrated sedimentological, mineralogical and geochemical investigation of the mineral siderite hosted in dark grey shale and sideritic concretions of Early Aptian (coeval with Oceanic Anoxic Event 1a) from the Tibetan Himalaya. Siderite is present throughout the section and possesses similar morphological characteristics whether in dark grey shale or concretions. Siderite can be present as disseminated and rhombic crystals formed during early diagenesis, or minor spherical crystals formed during late diagenesis. The evidence from redox elements, middle rare-earth element bulge patterns and extremely low carbon-isotope values of the sideritic concretions indicates that the iron carbonate was formed in the Fe-reduction zones by the process of dissimilatory iron reduction. This process would have required conditions of low $[SO_4^{2-}]$, reducing environment, abundant iron and high alkalinity. Additionally, the coexistence of siderite and pyrite may indicate that dissimilatory iron reduction occurred close to the microbial sulphate reduction zone, with seawater $[SO_4^{2-}]$ hovering around the tipping point at which pyrite could form once seawater sulphate increased. Such an increase during Oceanic Anoxic Event 1a could have resulted from basalt–seawater interaction and associated enhanced continental weathering, and/or hydrothermal activity. This study's observations support the previous hypothesis that low $[SO_4^{2-}]$ for Oceanic Anoxic Event 1a was probably caused by massive gypsum burial in the proto-South Atlantic. Subsequently, enhanced sulphate input could have promoted microbial sulphate reduction and accompanying oxidation of organic matter, which likely further enhanced nutrient recycling, increased primary productivity and organic-carbon burial, leading to more oxygen consumption and expansion of oxygen minimum zones, as reconstructed for many oceanic anoxic events.

Keywords Aptian OAE 1a, dark grey shale, low sulphate ocean, siderite, Tibetan Himalaya.

INTRODUCTION

There were several oceanic anoxic events (OAEs) and/or hyperthermals before and during the Mesozoic Era, including the Permian–Triassic Boundary Event (PTB; *ca* 252 Ma), the Triassic–Jurassic Boundary Event (TJB; *ca* 200 Ma), the Early Jurassic Toarcian OAE (T-OAE; *ca* 183 Ma), the Early Cretaceous Aptian OAE (OAE 1a; *ca* 120 Ma) and the Cenomanian–Turonian Boundary Event (OAE 2; *ca* 94 Ma) (e.g. Jenkyns, 2003, 2010; Hu *et al.*, 2020). These OAEs were generally associated with basalt–seawater interaction, rapid global warming, enhanced continental and marine weathering, ocean acidification, biological crises, accelerated hydrological cycles and expanded oceanic anoxia (Jenkyns, 2010; Foster *et al.*, 2018; Clapham & Renne, 2019; Hu *et al.*, 2020). These OAEs and related phenomena are generally linked in time to massive release, into the ocean–atmosphere system, of isotopically light carbon from greenhouse gases due to emplacement of large igneous provinces (LIPs), the dissociation of methane hydrate and/or the massive decomposition of terrestrial organic matter. There are, however, differences in the characteristics of the carbon-isotope perturbation in terms of duration and sign as well as magnitude of associated temperature increase (Jenkyns, 2010; Foster *et al.*, 2018; Hu *et al.*, 2020), likely to have been even more pronounced during Palaeozoic OAEs (Reershemius & Planavsky, 2021).

Studies have shown that low seawater sulphate concentrations ($[SO_4^{2-}]$) are also a common feature of Mesozoic OAEs (Ohkouchi *et al.*, 1999; Wortmann & Chernyavsky, 2007; Owens *et al.*, 2013; Algeo *et al.*, 2015; Gomes *et al.*, 2016; He *et al.*, 2020; Han *et al.*, 2022; Bauer *et al.*, 2022a). The pervasive low seawater $[SO_4^{2-}]$ has been suggested to have played an important role in the formation and evolution of OAEs by regulating the limiting nutrient supply of phosphorus (Adams *et al.*, 2010; Gomes *et al.*, 2016) and furthering anaerobic oxidation of methane (AOM; Luo *et al.*, 2010; He *et al.*, 2020). However, the case for low $[SO_4^{2-}]$ during OAEs is primarily based on modelling (Gomes *et al.*, 2016; Mills *et al.*, 2017; He *et al.*, 2020; Han *et al.*, 2022), with little direct sedimentological evidence. To date, the sediments of the T-OAE interval from the Mochras borehole of the Cardigan Bay Basin in Wales (Xu *et al.*, 2018) and of the OAE 1a interval from the Cismon (north Italy) drill core of the western Tethys and Deep Sea Drilling Project (DSDP) Site 463 in the Pacific (Bauer *et al.*, 2022a) have been reported as containing siderite ($FeCO_3$) as the sedimentary expression of low seawater $[SO_4^{2-}]$. Importantly, the formation of this mineral requires low seawater $[SO_4^{2-}]$ and appropriate conditions of relatively low oxygen, significant carbonate ion activity and iron-rich sediment and porewaters (e.g. Curtis & Spears, 1968; Ohmoto *et al.*, 2004). Although siderite is an effective proxy for redox conditions and biogeochemical cycles with respect to carbon, sulphate and iron (Berner, 1981; Ohmoto *et al.*, 2004; Romanek *et al.*, 2009), its changes in morphology and genesis as the OAE evolved potentially has implications for the global carbon cycle.

Among the well-studied OAEs mentioned above, OAE 1a is linked to the volcanic activity of Ontong Java Plateau (Kump & Arthur, 1999; Tejada *et al.*, 2009; Keller *et al.*, 2011; Erba *et al.*, 2015; Socorro *et al.*, 2017). OAE 1a started with a brief and pronounced $\delta^{13}C$ negative excursion taken to define its onset and believed to reflect a major carbon-cycle perturbation that was caused by a massive release of ^{13}C–depleted carbon into the ocean–atmosphere reservoir (e.g. Jenkyns, 2003, 2018; Erba *et al.*, 2010; Chen *et al.*, 2017). A subsequent $\delta^{13}C$ positive excursion was taken as evidence of a direct link with episodes of increased organic-carbon burial with deposition of dark grey shales followed by a stable plateau of persistent positive $\delta^{13}C$ values before returning to pre-event levels (Menegatti *et al.*, 1998; Bodin *et al.*, 2013).

In the Tibetan Himalaya, ammonite biostratigraphy as well as the characteristic carbon-isotope signature of OAE 1a has allowed identification of the sedimentary interval recording this event in the Gucuo II section (Chen *et al.*, 2017). Recent work found that abundant and stratigraphically continuous siderite was present in the dark grey shales and their associated concretions in this section. This study presents sedimentological, mineralogical and geochemical

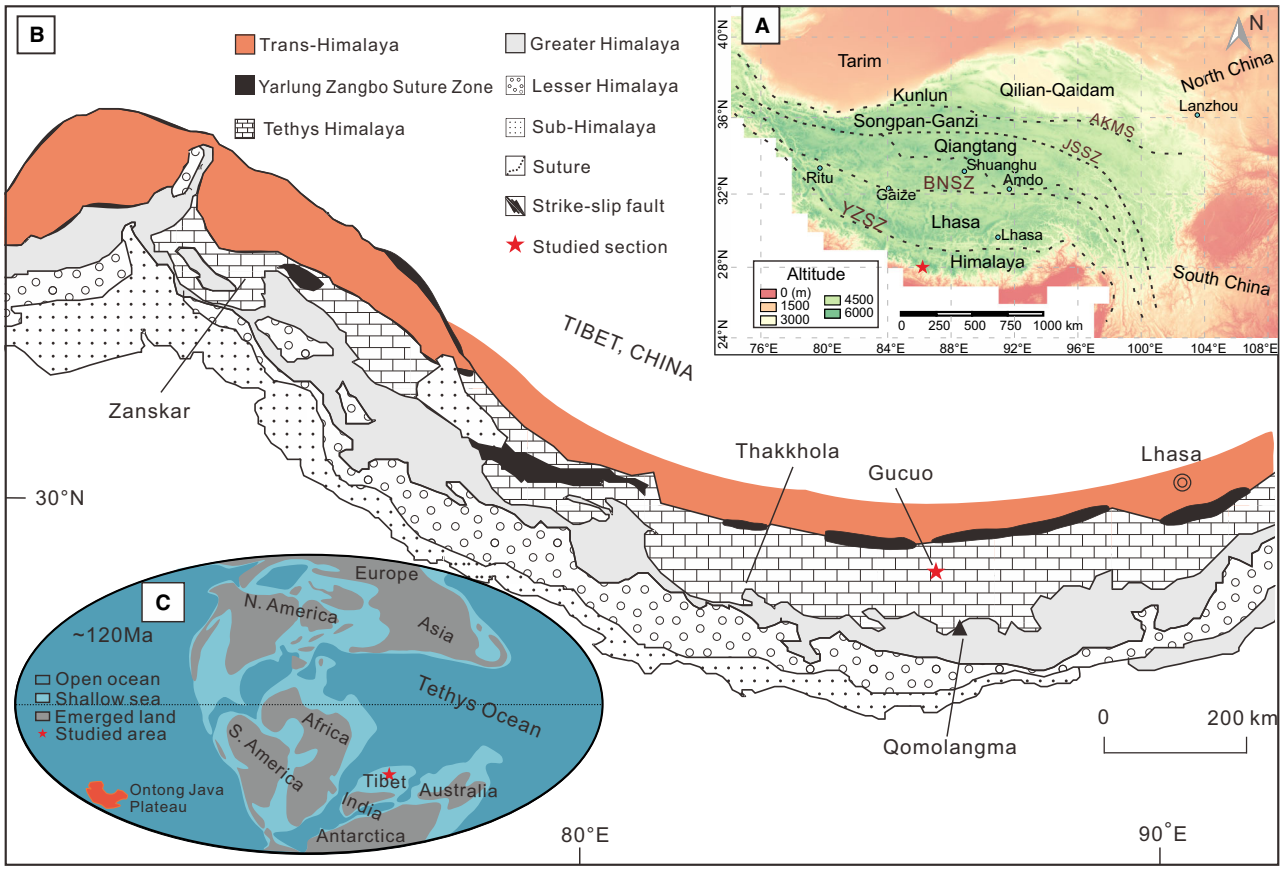

Fig. 1. (A) Digital elevation map showing the major blocks and sutures in the Tibetan Plateau. AKMS: Ayimaqin–Kunlun Suture Zone; JSSZ: Jinsha Suture Zone; BNSZ: Bangong–Nujiang Suture Zone; YZSZ: Yarlung Zangbo Suture Zone. (B) Geological sketch map of the Himalayas (modified from Gansser, 1964) and location of studied area. The red star marks the location of the Gucuo II section. (C) Early Aptian palaeogeographical map (*ca* 120 Ma; Scotese & Golanka, 1997), showing the location of the study area in the Tethys Himalaya.

data from the Lower Aptian dark grey shales and associated siderite to explore their significance for the formation and nature of OAEs.

GEOLOGICAL SETTING

The Himalayas are a nearly east–west-trending tectonic belt located in southern Tibet (Fig. 1A). This terrane is divided into the Sub-Himalaya, Lesser Himalaya, Greater Himalaya and Tethys Himalaya from south to north (Fig. 1B). The Tethys Himalaya is now located between the Greater Himalaya to the south and Yarlung Zangbo Suture Zone to the north. This belt comprises a complete Mesozoic succession, originally representing the deposits of the northern margins of the Indian continent (Fig. 1C), which can be divided into northern and southern subzones by the Gyirong–Kangmar Thrust; the northern zone is characterized by deep-water deposits, whereas the southern zone is dominated by shallow-water sediments (Liu & Einsele, 1994; Jadoul *et al.*, 1998; Han *et al.*, 2016).

The studied Gucuo II section (GPS: 28°44′46.44″ N, 86°18′46.68″ E) is located in the southern zone of the Tethys Himalaya (Fig. 1B). The lithostratigraphic unit of the Gucuo II section is the Lower Cretaceous Gucuo Formation, which is dominated by dark grey shale alternating with lighter coloured silty mudstone and shale intercalated with volcaniclastics and locally cut by clastic dykes. Ammonite and foraminiferal biostratigraphy and detrital zircon U–Pb ages, indicate that the age of the Gucuo Formation is Aptian and Albian (Hu *et al.*, 2008; Chen *et al.*, 2017). On the basis of age constraints, Chen *et al.* (2017) used organic-carbon

isotopes to confirm the presence of the OAE 1a interval of the Early Aptian in this section. The profile of the carbon isotopes was divided into six intervals (Fig. 2). In particular, the characteristic intervals 4 (*ca* 55 to 60 m) and 5 (*ca* 60 to 70 m) were thought to record the large negative and ensuing positive carbon-isotope excursion at the onset and recovery phase of OAE 1a (Chen *et al.*, 2017). This chemostratigraphic signature was thought to be the response to increased isotopically light carbon release and subsequent globally enhanced organic-matter burial, which was linked to the impact of Ontong Java volcanic activity (Keller *et al.*, 2011; Erba *et al.*, 2015).

MATERIALS AND METHODS

Scanning electron microscopy (SEM) and energy dispersive spectroscopy (EDS) analysis

Fifty-seven samples collected in the Gucuo II section were analysed microscopically, and 21 samples were investigated by SEM and electron detector. Samples were coated with *ca* 4 nm thick platinum for electric conduction before analysis. The microanalysis of the samples was performed at Chengdu University of Technology (Chengdu, China), using a field emission environment scanning electron microscope (FEI Quanta 250 FEG-SEM; Thermo Fisher Scientific, Waltham, MA, USA) with a working distance of 10 mm, and an accelerating voltage scanning of 20 kV; the SE2 probe and AsB detector were used for topography imaging and back-scattered component imaging, respectively. Quantitative analysis of components was carried out using an Oxford X-act energy spectrometer (Oxford Instruments, Abingdon, UK) connected to an electron microscope. The acceleration voltage was 20 kV, the working distance was 15 mm, and the diameter of the signal acquisition area was about 2 μm. Electron backscatter diffraction (EBSD) analysis was used for mineral phase identification, performed by an Oxford EBSD coupled to the field emission scanning electron microscope.

Carbon isotopes

Two concretions whose margins were enriched in siderite were selected to be powdered using a microdrill while taking care to avoid cement-filled veins and pores. Powders were dissolved in purified phosphoric acid (H_3PO_4) and the produced CO_2 was measured for isotope ratios by a Finnigan MAT Delta Plus XP mass spectrometer coupled to an in-line GasBench II auto sampler (Thermo Fisher Scientific) at Nanjing University (Nanjing, China). Results are reported in the standard delta notation in per mil deviation from the Vienna Pee Dee Belemnite (VPDB) standard. The analytical precision was better than 0.1‰.

Major and trace elements

Major and trace element analyses were performed at Nanjing University. Fused glass sheet was prepared by thoroughly mixing 1 g powdered samples with 11 g of a co-solvent ($Li_2B_4O_7$/$LiBO_2$/LiBr: 49.75%/49.75%/0.50%) before melting in platinum crucibles using a fully automatic electric melting furnace (THEOX; Malvern Panalytical, UK) operating at 40 kV and 75 mA. The sample analyses were determined using wavelength-dispersive X-ray fluorescence spectrometry techniques (ARL9900 XRF, Thermo Fisher Scientific) with two geological standards (BHVO-2 and BCR-2) being used to monitor data quality. The analytical accuracy {[(measured value − true value)/true value] × 100%} was verified by analysing these two standards and was better than 1.0% for oxide contents >1.0%, but better than 10% for oxide contents <1.0%. The analytical precision (reported as 1 sigma RSD) of the analyses was better than 5%.

Trace elements were analysed using a brief experimental process that can be described as follows.

1 50 mg powders of each sample were weighed and placed into PTFE (poly-tetra fluoroethylene) inner cans, dissolved with 1.5 mL of concentrated HF, and then evaporated to a nearly dry condition on a hotplate (130°C).

2 1.5 mL of concentrated HF and 1 mL of concentrated HNO_3 were added into the cans, which were then re-sealed in steel jackets and heated at 190°C in an oven for 72 h.

3 After cooling, the jackets were opened and evaporated at 130°C to a nearly dry condition on a hotplate. This evaporation process was repeated twice while adding 1 mL of concentrated HNO_3.

4 The resultant residues were re-dissolved with 1 mL of concentrated HNO_3 and 2 mL of H_2O, then sealed and heated in the steel jacket at 190°C for 12 h in the oven.

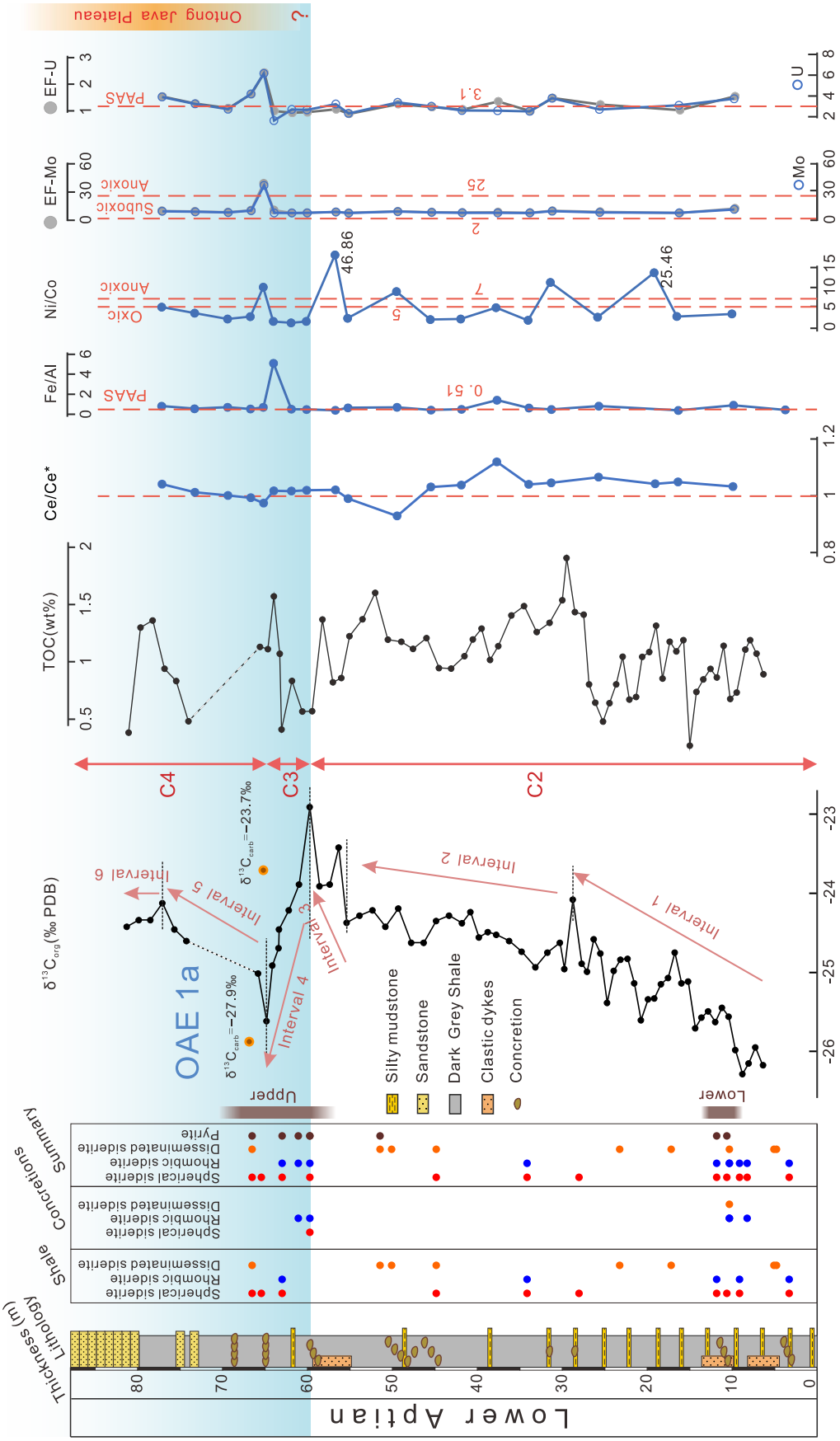

Fig. 2. Stratigraphic distribution of siderite and pyrite, organic-carbon isotopes ($\delta^{13}C_{org}$), characteristic $\delta^{13}C_{org}$ segments, total organic carbon (TOC), Ce/Ce*, Fe/Al, Ni/Co, Mo (EF-Mo) and U (EF-U). The $\delta^{13}C_{org}$ data and segments are from Chen *et al.* (2017). The blue shaded area marks OAE 1a and the orange segment indicates the interval of intense activity of the Ontong Java large igneous province (Erba *et al.*, 2015; Jenkyns, 2018). The thresholds of Fe/Al, Ni/Co, Mo and U are modified from McLennan (1989), Jones & Manning (1994) and Scott & Lyons (2012).

5 After it cooled down, the solution from step 4 was transferred to a polyethylene bottle to which was added 1 mL of a 500 ng/mL Rh internal standard solution to be diluted to 50 mL for ICP-MS analysis. The analytical precision was typically better than 5% (1 RSD), determined by analysis of two international rock standards and two duplicate samples ($n = 15$).

RESULTS

Siderite characteristics in the field and under the microscope

The lithology of the Gucuo II section is dominated by dark grey shale (Fig. 3A to C). Most of the concretions observed in the field are *ca* 3 to 7 cm in length, generally with a layered ring structure which can be roughly divided into two parts. The inside of the concretion is composed of a clay-rich mineral manifested as a weathered brown core in field observation (Fig. 3D and E) but fresh dark grey in polished slabs (Fig. 3F and G). These concretions are enclosed in dark grey shale layers (Fig. 3D and E). The sedimentological evidence from microscopic studies and inspection of polished slabs shows that siderite is concentrated in the outer ring of the concretions (Fig. 3F to H). Carbonate minerals, mainly siderite with minor calcite, are present outside the concretion in the dark grey shales.

A total of 16 samples of dark grey shale and five concretions hosted in dark grey shales were used to analyse the main composition of the siderite particles using SEM and EDS, and the results are shown in Table S1. All of these samples contain pure siderite with a content of 90.7 to 100 mol% $FeCO_3$ (99.16 ± 1.28 mol%, $n = 21$) and contain negligible $CaCO_3$, $MgCO_3$ and $MnCO_3$. Siderite is widely distributed both in the dark grey shales and concretions throughout the Gucuo II section. According to their morphological characteristics observed under the microscope, the siderite can be divided into three categories.

1 *Spherical siderite*. It is composed of an aggregation of siderite microspheres with a ring structure (mostly 0.1 to 1.0 μm in size; Fig. 4A), and the shape of aggregated spherulites ranges from irregular to spherical (Fig. 4B and C), similar to framboidal pyrite.

2 *Rhombic siderite*. Most of the rhombs are *ca* 5 to 20 μm in length, and some show traces of dissolution (or incomplete particle formation; Fig. 4D).

3 *Disseminated siderite*. It is dominated by siderite cements, which are distributed in shale pores and edges of clay minerals or is present in shale fissures (Fig. 4E and F). These different types of siderite can be observed in the same sample (Fig. 4G) and some of them occur with organic matter (Fig. 4H and I).

Pyrite characteristics under the microscope

The samples from two intervals (*ca* 10 to 12 m and *ca* 50 to 70 m) contain pyrite, with the mineral grains being less than 1 μm in diameter (Figs 2 and 4J to L). The pyrites all coexist with siderite. Rare pyrite grains in the lower interval (*ca* 10 to 12 m) are observed in siderite cores under the high magnification of the SEM. The upper interval (*ca* 50 to 70 m) contains more abundant pyrite than the lower interval; the mineral has either grown individually (Fig. 4J) or coexists with siderite (Fig. 4K and L).

Carbon-isotope values of concretions

Carbon-isotope measurements were carried out on two concretions. The carbon-isotope value of two samples at 65.9 m and 67.4 m are −23.7‰ and −27.9‰, respectively.

Major and trace elements

Twenty-one dark grey shale samples and two concretions were analysed for major and trace elements, and the results are shown in Tables S2 and S3 and described (average ± std) below. Rare-earth elements (REE) are normalized to Post Archean Australian Shale (PAAS; McLennan, 1989) and the REE pattern of concretions and dark grey shales is shown in Fig. 5. The total REE concentrations range from 136.07 to 625.15 ppm (351.23 ± 140.93 ppm) of the dark grey shales, 55.66 ppm and 71.78 ppm of the two concretions. The REE pattern shows light REE (LREE) depletion, middle REE (MREE) enrichment and heavy REE (HREE) depletion. Dark grey shales have an Fe_2O_3 content of 3.04 to 21.34 wt.% (6.56 ± 4.08 wt.%), which is lower than PAAS (7.23 wt.%; McLennan, 1989). The Al_2O_3 concentrations are 4.67 to 19.11 wt.% (14.76 ± 3.30 wt.%), which is also lower than PAAS (18.90 wt.%; McLennan, 1989). Consequently, samples have Fe/Al ratios of 0.24 to 6.04 (0.79 ± 1.23), higher than PAAS (0.51;

McLennan, 1989). The value of Ce anomalies is 0.87 to 1.13 (1.05 ± 0.07) and of Ni/Co is 0.84 to 46.86 (6.82 ± 11.01). To eliminate the effects of dilution by detrital flux when reconstructing redox conditions, enrichment factors (EF: $EF_{element\ X} = X/Al_{sample}/X/Al_{average\ shale}$) are used to describe the degree of element enrichment in sediments. Generally, an abundance of Mo above the crustal average (2 ppm) and below 25 ppm indicates a non-euxinic setting where H_2S was restricted to the porewaters; values between 25 ppm and 100 ppm represent an intermittently euxinic setting or permanently Mo-depleted euxinic setting, and greater than 100 ppm records permanently euxinic, Mo-replete settings (Scott & Lyons, 2012). The key redox elements for the ten dark grey shale samples are as follows: values of Mo concentration are 0.86 to 66.33 ppm (6.78 ± 15.82 ppm); of EF-Mo is 1.10 to 65.57 (7.43 ± 15.70); of U is 0.61 to 6.43 ppm (2.76 ± 1.45 ppm); of EF-U is 0.70 to 2.20 (1.10 ± 0.40). These data and threshold values for redox proxies mentioned above are plotted in Fig. 2.

DISCUSSION

Redox conditions

According to the oxygen content of bottom water, the redox conditions can be divided into oxic, suboxic and anoxic (Fig. 6A; Tyson & Pearson, 1991; Canfield & Thamdrup, 2009; Petrash *et al.*, 2017). Some redox-sensitive elements are more soluble under oxidizing conditions than reducing conditions, such as Mo, U and Co, and they tend to be more enriched in anoxic environments (Tribovillard *et al.*, 2006, 2012). Molybdenum exists in the form of molybdate (MoO_4^{2-}) in oxidizing seawater and has high concentrations, which can only be adsorbed by Mn-Fe (oxyhydr)oxides (Barling & Anbar, 2004). By contrast, Mo can be reduced to MoS_4^{2-} under anoxic to euxinic conditions and then enriched in sediments by absorption into organic matter or Fe sulphide minerals (Helz *et al.*, 2011). Uranium exists as a dissolved phase in the conservative form of hexavalent uranyl ions ($UO_2(CO_2)_3^{4-}$) in oxic seawater where the dissolved U cannot be scavenged by particulates (Tribovillard *et al.*, 2006). The reduction of U can occur under reducing conditions in a similar way to Fe (Morford *et al.*, 2001; Poulson *et al.*, 2006) and, unlike Mo, the resultant reduced products (UO_2, U_3O_7 and U_3O_8) can be absorbed and enriched in sediments, rather than ferromanganese oxides (Tribovillard *et al.*, 2006). Therefore, changes in U (EF-U) and Mo (EF-Mo) in sediments can reflect redox conditions in seawater.

Iron from deep-sea sediment porewaters, hydrothermal fluids (Poulton & Canfield, 2011) and/or oxic shelves (Anderson & Raiswell, 2004) can be enriched in anoxic marine conditions, and thus Fe/Al ratios can enable anoxic and oxic depositional environments to be distinguished (Lyons & Severmann, 2006; Raiswell & Canfield, 2012). The Ni/Co ratio is also commonly used as a redox indicator. When the value of Ni/Co is less than 5, between 5 and 7, and greater than 7, it suggests oxygenated, weakly oxygenated and anoxic conditions, respectively (Jones & Manning, 1994). Additionally, under suboxic conditions, Fe-Mn oxide/-hydroxide will dissolve, resulting in insoluble Ce^{4+} being reduced to soluble Ce^{3+}, leading to Ce enrichment in seawater and corresponding Ce depletion in sediments (cf. Tostevin, 2021). The value of Ce anomalies is derived from the formula $(Ce/Ce^*)_N = Ce_N/(Pr_N{*}Pr_N/Nd_N)$ proposed by Lawrence *et al.* (2006). The thresholds of each redox proxy mentioned above have been illustrated in Fig. 2.

In the Gucuo II section, the Fe/Al, Mo (EF-Mo) and U (EF-U) data show relatively stable

Fig. 3. Field photographs, microphotographs of dark grey shales and concretions from the Gucuo II section. (A) Field photographs showing the lithological unit 1 and unit 2 of the Gucuo II section (cf. Chen *et al.*, 2017). (B) Close-up photographs of dark grey shales from unit 2. (C) Typical dark grey shale under cross-polarized light (35.5 m). (D) Siderite concretions having ring structure (red dashed circles) within dark grey shales. (E) Siderite concretions growing along the dark grey shale layers. (F) Polished slab of sideritic concretion (67.4 m). The red circle represents the location where $FeCO_3$ is concentrated, and powders extracted to analyse the carbon isotopes. The inner and outer ring are dominated by clay minerals (Cm) and carbonate (Cb). (G) Polished slab of sideritic concretion (65.9 m), showing typical concentric growth model with siderite grains concentrated on the outside layer of the concretion. (H) Microphotograph showing details of the transitional part from middle to the layer marked on (G) (65.9 m; crossed polars).

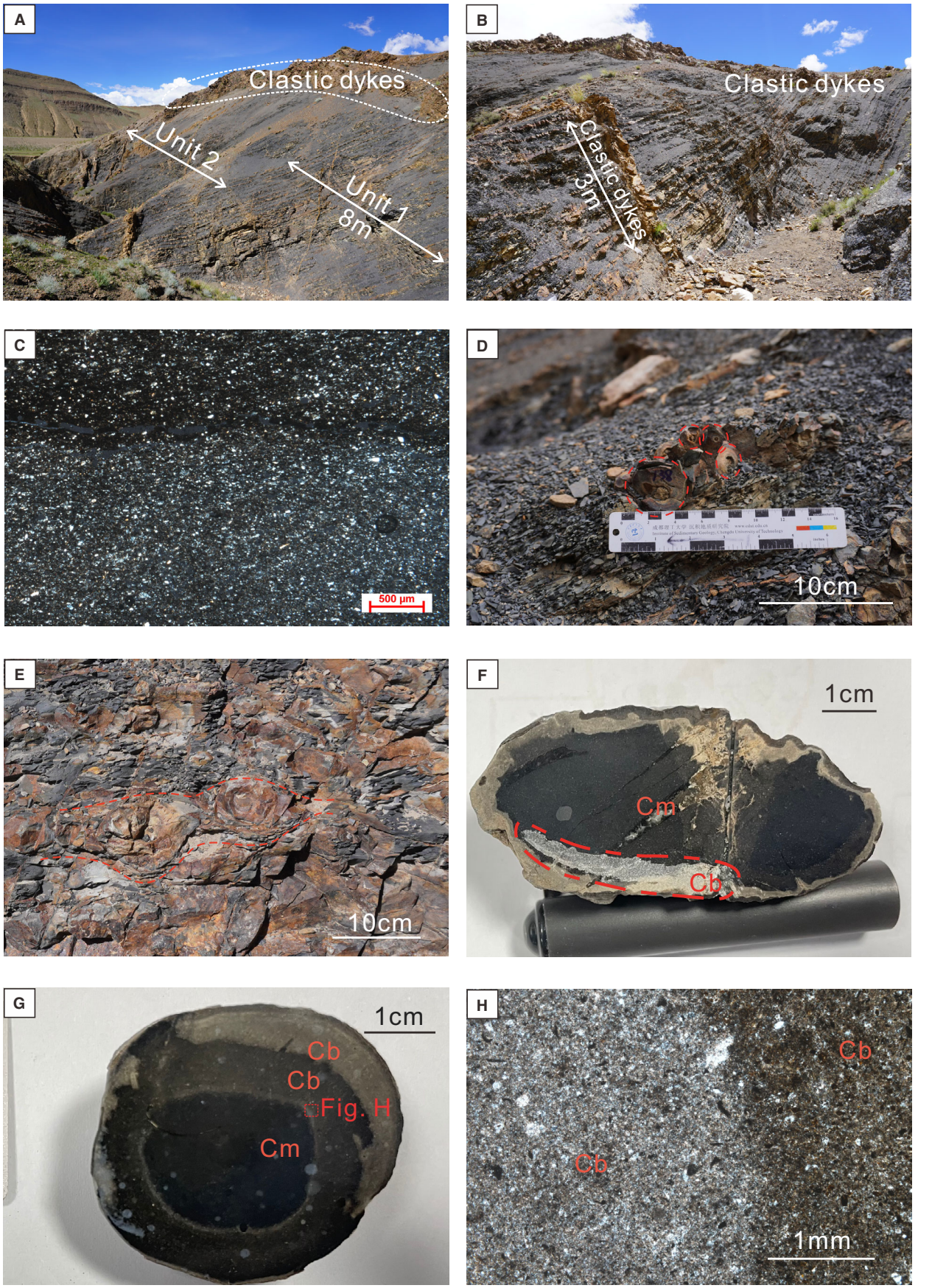

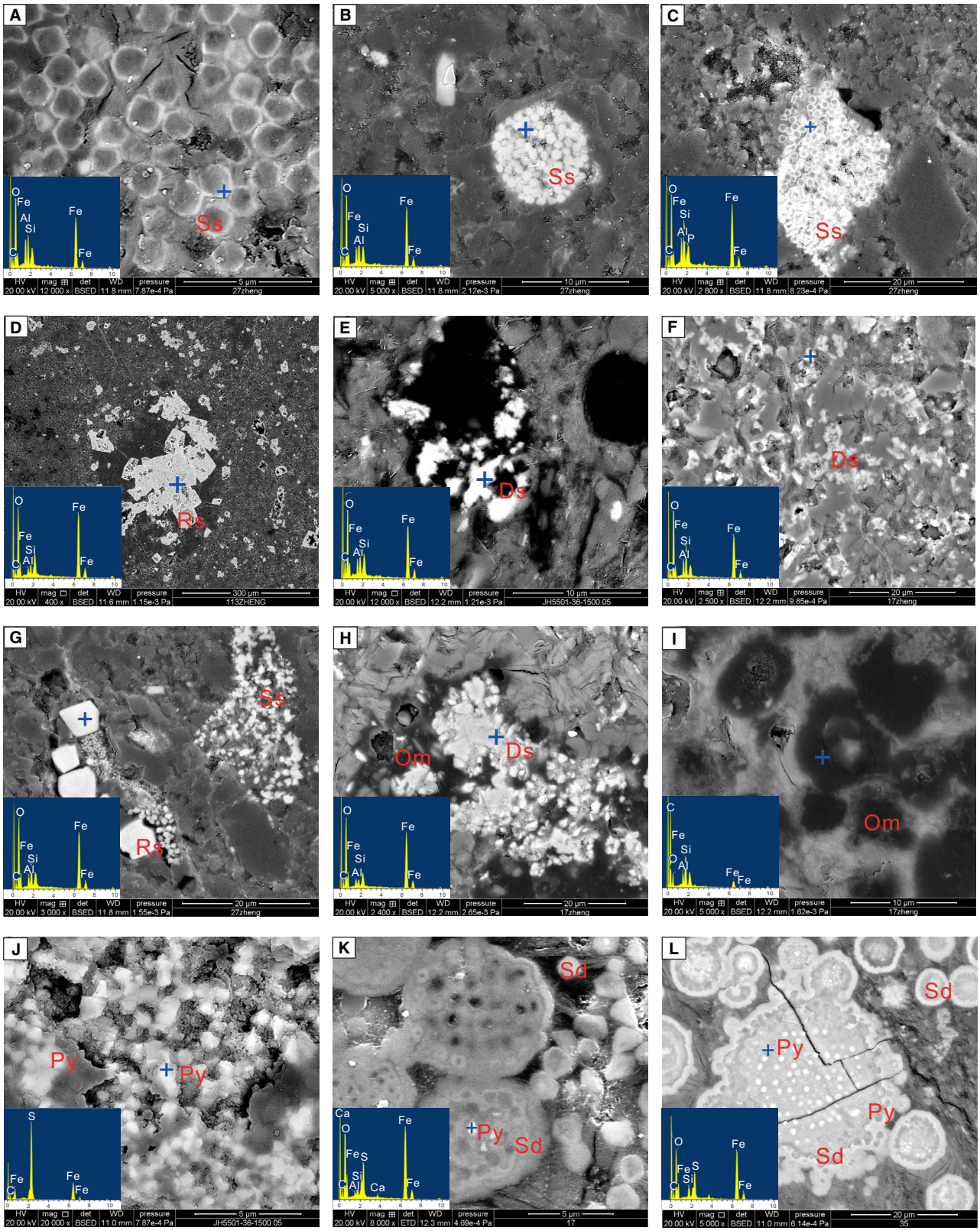

Fig. 4. Scanning electron microscopy (SEM) images and energy dispersive spectroscopy (EDS) spectrum (point '+') of typical siderite and pyrite from the dark grey shales. (A) Spherical siderite (Ss; 10.08 m). Each microsphere has edge (bright) and core (dark). (B) Spherical siderite aggregate, similar to the pyrite (Py) framboid (10.08 m). (C) Irregular aggregate of spherical siderite microspheres (10.08 m). (D) Aggregate of rhombic siderite (Rs) (37.68 m). (E) Disseminated crystals or cementation by siderite (white) in the pores (5.28 m). (F) Disseminated crystals (Ds) and/or cementation by siderite (the white) in the fissure (5.61 m). (G) Aggregate of rhombic and spherical siderite in the same field of view (10.08 m). (H) and (I) Siderite aggregates surrounded by black organic matter (Om) (5.61 m). (J) Clustered spherical pyrite grains occurring without siderite (67.4 m). (K) Spherical pyrite occurring in the core of siderite (13.05 m). (L) Clustered spherical pyrite grains (resembling pyrite framboids) located in the inner part of a siderite mass (69.5 m).

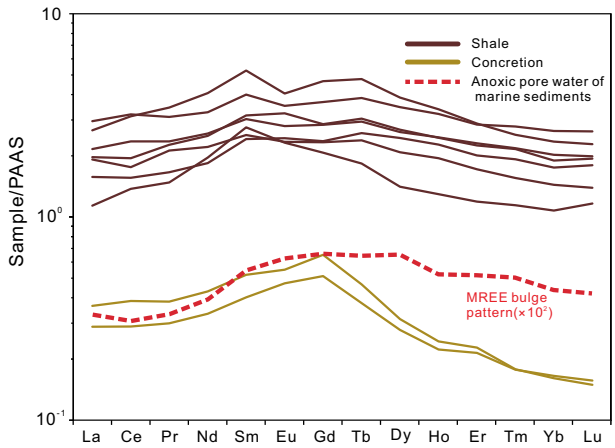

Fig. 5. Post Archean Australian Shale (PAAS)-normalized REE distributions of the shales and sideritic concretions in this study. The PAAS data are from McLennan (1989) and rare-earth element (REE) pattern with distinct MREE enrichment (MREE-bulge or hat-shaped distribution) from anoxic porewaters of marine sediments is modified from Haley *et al.* (2004).

values hovering closely around the oxic–suboxic threshold (Fig. 2). By contrast, the Ce/Ce* and Ni/Co data are somewhat scattered, and a few datapoints even reach the obvious oxic and anoxic zones. Together with the additional evidence of modest total organic carbon (TOC) values ranging from 0.5 to 1.5% (Chen *et al.*, 2017), the Gucuo II section could have been mainly deposited in a suboxic setting (ferruginous conditions). This conclusion is supported by the relative enrichment of MREE observed in both concretions and dark grey shales (Fig. 5), which points to the DIR process under ferruginous conditions because the dissolution of Fe oxides/oxyhydroxides could have released MREEs to the porewaters, thereby imparting a distinctive 'MREE bulge' (German & Elderfield, 1989; Haley *et al.*, 2004). Notably, interval 4 (*ca* 65 to 70 m) shows positive pulses in Fe/Al, Ni/Co, EF(EF-Mo) and U(EF-U), likely indicating transient fluctuations to more oxygen-depleted (anoxic) conditions. Such a redox pattern is supported by the pulse in TOC increase (Chen *et al.*, 2017; Fig. 2) and newly reported high-resolution redox data (EF-Mo, EF-U and Th/U) that also show their enrichment of key proxies in interval 4 (Nie *et al.*, 2023).

Stage and genesis of the lower Aptian siderite and pyrite

Siderite is potentially an important proxy because of the specific conditions for its formation: anoxic environments, low [SO_4^{2-}], sufficient ferrous iron and high alkalinity (Curtis & Spears, 1968; Berner, 1981; Ohmoto *et al.*, 2004; Romanek *et al.*, 2009). In essence, oxic conditions are favourable for the formation of Fe (oxyhydr)oxides, while high [SO_4^{2-}] and a sulphidic environment favour the formation of sulphide minerals such as pyrite. By contrast, ferruginous conditions, occupying an intermediate redox window between oxic and sulphidic, are favourable for siderite formation under conditions of low [SO_4^{2-}]. For instance, it may be noted that siderite is one of the most typical minerals found in Precambrian banded iron formations due to the dominance of ferruginous oceans (Ohmoto *et al.*, 2004; Bekker *et al.*, 2010; Heimann *et al.*, 2010).

To date, the genesis of siderite has been explained in the following ways: (i) direct precipitation from seawater during the syn-depositional stage (e.g. Berner, 1981; Heimann *et al.*, 2010); (ii) authigenic precipitation from porewater facilitated by DIR or methanogenesis during early diagenesis (Garcia *et al.*, 2016; Tang *et al.*, 2018); and (iii) formation by reduction of ferric minerals together with

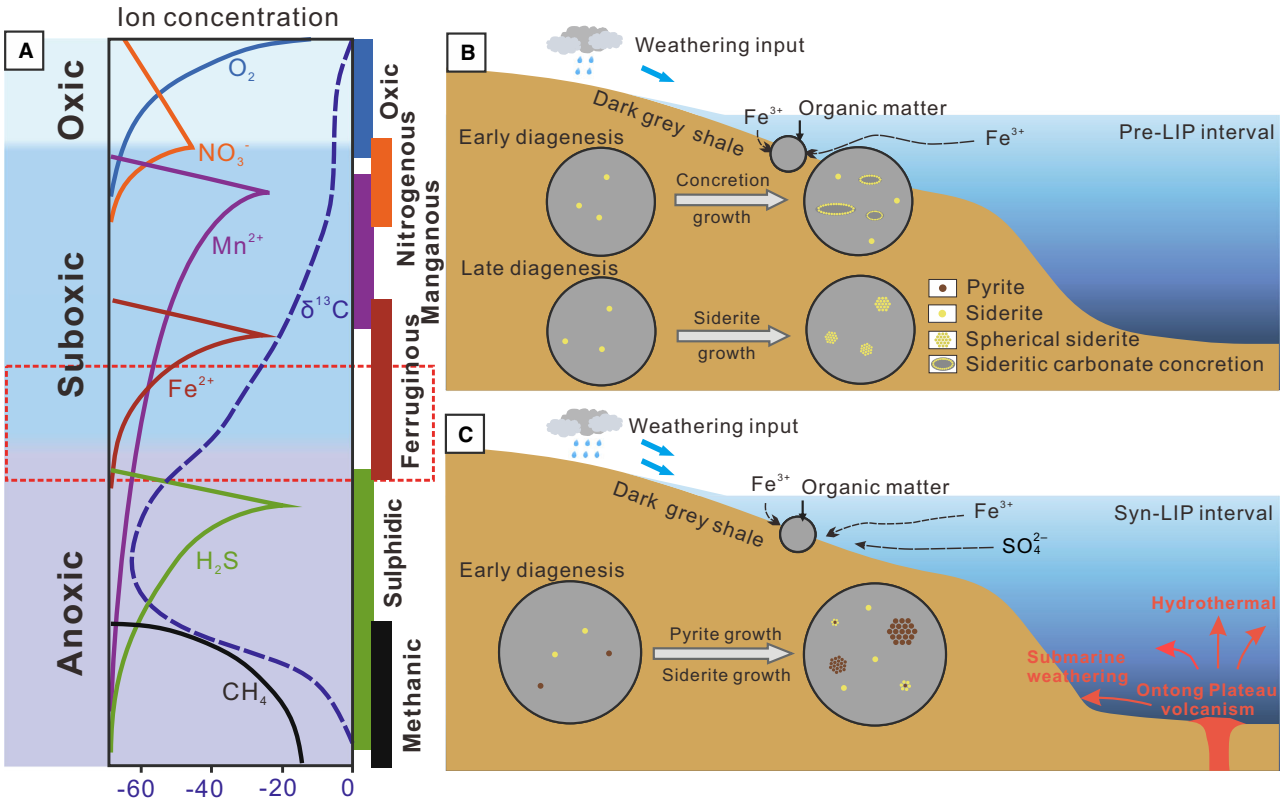

Fig. 6. (A) Schematic illustration of early diagenetic environment with redox zones in marine sediment porewaters (adapted from Liu *et al.*, 2019). The iron reduction zone (marked by red rectangle in dashed line), likely mixed with the uppermost sulphate reduction zone, inferred to be the location where siderite and pyrite were deposited. (B) and (C) Model of siderite formation in dark grey shales and concretions under the conditions of low marine sulphate concentration. (B) The sulphate-depleted environment that was favourable for siderite formation before the activities of the Ontong Java large igneous province (LIP). (C) A more sulphate-rich environment than that of (B), likely related to the extrusion of the Ontong Java LIP and associated enhanced basalt–seawater interaction and continental weathering, that was able to form pyrite coexisting with siderite.

thermal decomposition of organic carbon at high burial temperature and pressure during late diagenesis (Köhler *et al.*, 2013; Halama *et al.*, 2016). In this study, siderite is observed both in concretions and dark grey shales throughout the Gucuo II section, which is interpreted as deposited in a generally suboxic environment, one of the basic conditions favourable for siderite formation. Therefore, further investigation of the genesis of siderite in the dark grey shales and dark grey shale-hosted concretions, particularly over the OAE 1a interval, is warranted.

Implications from the observations in the field and under the scanning electron microscope

Siderite-bearing concretions are authigenic mineral aggregates that occur commonly in sandstones and shales, especially in organic-rich mudstones (Raiswell, 1987; van der Weijden, 1992). Field investigations of the Gucuo II section show that these siderite concretions do not cut through the bedding and their curved geometry suggests that the relatively rigid bodies have grown displacively within the surrounding sediment, which has subsequently undergone significant differential compaction (Fig. 3E). This evidence indicates early diagenetic growth of concretions in the organic-rich shales. The polished slabs of concretions show a multi-layered ring structure. Taking Fig. 3G as an example, the dark grey component in the centre of the concretions is mainly clay minerals. Outer circles follow a bright–dark–bright pattern, but they are all primarily made of carbonate (mostly siderite with minor calcite), and the bright–dark difference can also be seen

under the SEM (Fig. 3H). This type of concretion generally forms during early diagenesis when large amounts of ferrous iron are released into the porewaters, and Fe reacts with CO_3^{2-} or HCO_3^-, thereby forming $FeCO_3$ (Mozley & Burns, 1993; Raiswell & Fisher, 2000; Gaines & Vorhies, 2016). Carbonate material is progressively added to the exterior of the concretionary bodies, and clay minerals are synchronously aggregated therein (Fig. 6B; Gaines & Vorhies, 2016), just as observed in the Gucuo II section (Fig. 3G). This type of displacive growth is prone to forming ring structures (Fig. 3D; Gaines & Vorhies, 2016; Liu *et al.*, 2019).

In addition to the siderite within concretions, there are three types of μm-scale siderite in the dark grey shale: disseminated, rhombic and spherical. Disseminated siderite mostly occurs in the pore spaces of dark grey shale (Fig. 4E) or in fissures as cements (Fig. 4F). Due to the limited growth space, siderite exhibits irregular crystal morphology and is generally interpreted as having formed in sediments that were buried and isolated from seawater, where primary particles [such as $Fe(OH)_3$] could interact with ions (such as HCO_3^-) in the interstitial water. If this siderite was not limited by growth space, its crystal form developed a rhombic shape (Fairbridge, 1967).

The shape of spherical siderite is very recognizable under the microscope, and each microsphere that makes up spherical aggregation of the mineral is very small (*ca* 1 to 2 μm; Fig. 4A to C). Previous studies have suggested that this morphology is evidence for the transformation of $Fe(OH)_3$ colloid particles into siderite that retains the primary spherical shape (Huang, 2004), and/or is derived from remnants of microbial cells formed in late diagenesis (LaBerge, 1973; Kaźmierczak, 1979; Köhler *et al.*, 2013). Recent studies have shown that, in the presence of Fe^{3+}, organic matter can undergo thermal decomposition, produce CO_2 and serve as an electron donor under conditions of more than 170°C and 1.2 kPa, generally during burial diagenesis when Fe^{3+} is reduced to Fe^{2+} (Köhler *et al.*, 2013; Halama *et al.*, 2016).

In summary, siderite within concretions and dark grey shales is present throughout the Gucuo II section. The concretions and dark grey shales both contain the early (disseminated and rhombic) and late (spherical) diagenetic siderites formed in the different pathways described above. Generally, complete post-depositional (burial) processes can be roughly divided into early (near-surface) and late (burial) diagenesis, followed locally by final metamorphism. The observations in this study unambiguously confirm that the samples were mainly affected by early and late diagenesis (see *Discussion* section above). Notably, the spherical siderites likely indicate deep-burial diagenesis (probably extending to several kilometres) because of the reconstructed high temperatures (more than 170°C). Such diagenetic processes could have preferentially decomposed the ^{12}C-enriched organic matter, which thus resulted in residual higher $\delta^{13}C_{org}$ values: a conclusion supported by the observation that the $\delta^{13}C_{org}$ of Gucuo II generally have higher values than those recorded in coeval sections of Cau in Spain and of DSDP Site 463 in the Pacific (Chen *et al.*, 2017). Although the Gucuo II section is located in the high tectonic zone of the Himalayan orogenic belt, which experienced high pressure and high temperature during large-scale tectonic processes, the sediments in the study area are relatively well-preserved and have not suffered metamorphism: a conclusion confirmed by the lack of metamorphic minerals in thin-sections (Fig. 3).

Implications from carbon isotopes and rare-earth element patterns

The composition of carbon isotopes in siderite is controlled by the different sources of HCO_3^--bearing fluid from microbial respiration of organic matter under suboxic to anoxic conditions (e.g. Sellés-Martínez, 1996; Loyd *et al.*, 2012) that, in turn, can be used to track the formation stage and growth mechanism of iron carbonate. As mentioned above, the formation of siderite generally requires rather precise conditions: namely, a low-oxygen, carbonate ion-rich and iron-rich environment. The oxygen-deficient methanogenic and suboxic zones are thus favourable for its formation (Fig. 6A; Mozley & Wersin, 1992). Within the methanogenic zone, organic matter is decomposed by microorganisms, which can produce $\delta^{13}C$-depleted methane but paired $\delta^{13}C$-enriched HCO_3^-, because this process preferentially utilizes ^{13}C-depleted carbon to synthesize methane (Raiswell & Fisher, 2004). Therefore, siderite usually has relatively high carbon-isotope values (even reaching *ca* 21.9‰) compared to those formed by the DIR process (Krylov *et al.*, 2008) due to the combination of $\delta^{13}C$-enriched bicarbonate and ferrous ions by the following processes:

$$CH_3COOH = CH_4 + CO_2 \quad (1)$$

$$CO_2 + H_2O = HCO_3^- + H^+ \quad (2)$$

$$Fe^{2+} + 2HCO_3^- = FeCO_3 + CO_2 + H_2O \quad (3)$$

By contrast, the DIR process mediated by iron-reducing bacteria is widespread in the suboxic zone (Fig. 6A), where the Fe-oxyhydr(oxides) are acceptors of electrons from organic-matter oxidation, with siderite being formed by reaction between bicarbonate and ferrous ions [$4Fe(OH)_3 + CH_2O + 3HCO_3^- = 4FeCO_3 + 3OH^- + 7H_2O$]. Such a process is relatively common during early diagenesis (Lovley, 1991; Konhauser *et al.*, 2005; Heimann *et al.*, 2010; Teixeira *et al.*, 2017; Tang *et al.*, 2018). Thus, the carbon-isotope ratios of siderite formed by DIR are mainly inherited from low values of decomposing organic matter (−20 to −25‰). Modification of these values from mixing with seawater derived from above the seafloor (*ca* 0‰) and/or mixing with waters from the sulphate-reduction zone deeper in the sediment pile (*ca* −25 to 0‰; Fig. 6A; Irwin *et al.*, 1977; Liang *et al.*, 2016), could have taken place due to migration of redox zones. The C–O–Fe-isotope mass-balance reaction pathways for siderite formation by DIR suggest that, if not affected by neighbouring redox zones, the $\delta^{13}C_{carb}$ of the mineral can inherit an isotopic signature from organic matter, with $\delta^{13}C$ values as low as −30‰. comparable to the source material (Heimann *et al.*, 2010).

In this study, the two analysed concretions in the Gucuo II section have $\delta^{13}C_{carb}$ of −23.7‰ and −27.9‰, respectively. These $\delta^{13}C_{carb}$ figures are very close to the range of organic $\delta^{13}C$ values (−25.02 ± 0.47‰; Chen *et al.*, 2017). Therefore, the carbon-isotope values of siderite were primarily inherited from that of the organic matter during the DIR process in the suboxic zone. This inferred geochemical pathway is also supported by the MREE bulge pattern (see interpretation above), and sedimentary and geochemical evidence that the Gucuo II section is dominated by dark grey shale with relatively high TOC content (Chen *et al.*, 2017). Notably, the BSE images show that the siderite commonly coexists with black organic matter (Fig. 4H and I). Such conditions could have been favourable for siderite formation directly using the HCO_3^- produced from *in situ* organic-matter decomposition and Fe^{2+} from DIR.

Implications from coexistence of siderite and pyrite

The pyrite, identified by EDS analysis, occurs randomly at submicron scale within the siderite grains and has apparently acted either as nuclei (*ca* 1 μm) for growth of the iron carbonate (Fig. 4K and L), or emerged individually (Fig. 4J). Based on the current data in this study, the associated siderite present in the concretions and enclosing dark grey shales shares common characteristics in morphology. The pyrite grains, as well as the coexisting siderite, could have formed in early diagenesis (cf. Wilkin *et al.*, 1996; Bond & Wignall, 2010), synchronously with the individual siderite grains (except in the case of the late diagenetic spherical siderite, as discussed above; Fig. 4K and L).

The formation of pyrite requires reduced sulphur (HS^-) from microbial sulphate reduction (MSR) and concomitantly reduced iron (Fe^{2+}) from DIR, which then react together (Fig. 6C; Wilkin *et al.*, 1996). By contrast, siderite generally forms in early diagenesis in response to low [SO_4^{2-}] under reducing conditions, with abundant iron and high alkalinity (Curtis & Spears, 1968; Berner, 1981; Ohmoto *et al.*, 2004; Romanek *et al.*, 2009). These observations and fundamental principles suggest overall sulphate depletion of marine waters favourable for siderite formation in the Early Aptian of the Tibetan area with, however, enough sulphate being made available for MSR and pyrite formation, in the pre-OAE 1a (*ca* 10 to 12 m) and syn-OAE 1a (*ca* 50 to 70 m) intervals (Fig. 2). Notably, the relatively rare occurrence and low proportion of pyrite also suggests pervasive marine low-sulphate concentrations that limited formation of iron sulphides. Based on the SEM and EDS observations of scattered pyrite grains and pyrite nuclei within the siderite, it is likely that the iron sulphide formed first during early diagenesis, a process that continually consumed sulphate until its concentration reached the lowest threshold for MSR. Subsequently, the extreme depletion of sulphate in the porewaters, coupled with additional Fe^{2+} availability, would, in the presence of CO_3^{2-}, have favoured formation of siderite that surrounded the earlier formed pyrite (Figs 4K, L and 6C). By contrast, the individual siderite aggregates likely formed subsequently when the HS^-, supplied by MSR in the porewaters, was completely consumed during early diagenesis. Notably, the coexistence of pyrite (in two intervals of *ca* 10 to 12 m and *ca*

50 to 70 m) and siderite (throughout the Gucuo II section) suggests that formation of the iron carbonate likely occurred in the lower iron reduction zone (the red rectangle; Fig. 6A), which could mix with the lower sulphate reduction zone. Moreover, the positive pulse of major redox proxies and relatively elevated TOC content in the upper interval also likely indicate a more reducing (anoxic) environment within the sediment (Fig. 2). This zone could have been favourable for siderite formation, and occasionally also favourable for pyrite when sulphate concentrations were high enough to foster MSR and produce HS^- due, for example, to pulses of sulphate input from enhanced continental weathering and/or volcanism.

In summary, the integrated evidence from siderite characteristics, $\delta^{13}C_{carb}$ data, REE patterns and coexisting siderite and pyrite suggest that: (i) the siderite with disseminated and rhombic crystals formed during early diagenesis, whereas the spherical siderite formed during late diagenesis, and these two morphological forms generally coexist together throughout the section; and (ii) the early diagenetic siderite and local coexisting pyrite formed by the DIR process point to the particular conditions of low $[SO_4^{2-}]$, reducing environment, abundant ion and high alkalinity. Significantly, dissolved sulphate in porewaters inherited from the overlying water column (seawater) could have been consumed by MSR, if conditions allowed, which could have decreased the sulphate concentrations in the pore fluids, thereby losing the original geochemical signature of seawater. However, as mentioned above, the DIR process was apparently dominant in porewater and minor amounts of pyrite were only observed in lower (*ca* 10 to 12 m) and upper (*ca* 50 to 70 m) intervals of the section (Fig. 2). These observations suggest that MSR and pyrite formation had negligible influence on the changes in sulphate concentration in porewaters, which thus likely represents the seawater signal.

Sulphate concentration changes in the early Aptian

In this study, early diagenetic siderite appears throughout the Gucuo II section including the pre-OAE 1a and syn-OAE 1a intervals. According to the Early Aptian carbon-isotope characteristics and pattern, Menegatti *et al.* (1998) divided the OAE 1a signature into eight segments (C1 to C8). In the Gucuo II section, Chen *et al.* (2017) used the biostratigraphy and carbon-isotope characteristics to perform a correlation with the typical eight segments of Menegatti *et al.* (1998), which suggests that the intervals 1 to 3 correspond to the upper C2 segment, interval 4 to C3, interval 5 to C4a–b, and interval 6 to 4c. In particular, the time duration of C3 (interval 4) and C4 (intervals 5 and 6) has been well-constrained by astronomical cyclostratigraphy and estimated to have lasted *ca* 1200 kyr in total (see review by Hu *et al.*, 2020, and references therein). Therefore, the total duration of intervals 1 to 6 should have been greater than *ca* 1200 kyr, thereby suggesting a long-term low in seawater $[SO_4^{2-}]$. Although the occurrence of pyrite in the two intervals of *ca* 10 to 12 m (pre-OAE 1a) and *ca* 50 to 70 m (syn-OAE 1a) suggests pulses of relative increase in sulphate input, their limited occurrence and proportion still indicate relatively low-sulphate concentrations that could have severely limited MSR and HS^- availability for pyrite formation. In particular, the elevated occurrence of pyrite over the syn-OAE 1a interval indicates higher marine sulphate concentrations and is broadly coincident with the time of emplacement of the Ontong Java LIP (Fig. 2). This inference is supported by most radiometric ages (*ca* 124 to 120 Ma) (Timm *et al.*, 2011) and sedimentary geochemical proxies (for example, Pb, Sr and Os isotopes, Hg concentrations, Mn and Eu/Eu*) (Bottini *et al.*, 2012; Erba *et al.*, 2015; Bauer *et al.*, 2021; Percival *et al.*, 2021) for the Ontong Java LIP, which indicates that the onset of volcanism was synchronous with the beginning of OAE 1a (C3; Fig. 2). Thus, the syn-OAE 1a increase in $[SO_4^{2-}]$ could be attributed to sulphate input from submarine volcanism and/or hydrothermal activity and associated enhanced continental/marine weathering (Fike *et al.*, 2015; Jenkyns, 2018). Furthermore, this occurrence of pyrite corresponds to a negative excursion of sulphur isotopes ($\delta^{34}S_{CAS}$) in carbonate-associated sulphate (CAS; Gomes *et al.*, 2016) that could be ascribed to input of relatively elevated volcanically derived ^{34}S-depleted sulphate from some form of basalt–seawater interaction. In addition, high-resolution geochemical proxies likely reflect multiple discrete pulsed volcanic episodes, including the intervals of C2 (before OAE 1a) and C3–C4 (during OAE 1a) (Gomes *et al.*, 2016; Bauer *et al.*, 2021). Based on the current carbon-isotope correlation (Chen *et al.*, 2017), the earlier LIP activity (pre-OAE 1a) was probably the cause of pyrite formation during

the interval of *ca* 10 to 12 m in Gucuo II. However, recent high-precision $^{40}Ar/^{39}Ar$ data from the Ontong Java LIP show an age range from 116.85 to 107.96 Ma, younger than previous dates mentioned above. These results, if accepted, show that the volcanism appears too young to have triggered OAE 1a. However, these ages could be ascribed to failure to recover the older volcanic stratigraphy from the available drilling record (Davidson *et al.*, 2023).

Overall, the integrated sedimentological, mineralogical and geochemical evidence indicates relatively low-sulphate concentrations in the marine waters of south-eastern Tethys (Southern Hemisphere) in the Early Aptian during the pre-OAE 1a and syn-OAE 1a intervals. Geographically restricted settings could have caused the composition of an isolated sulphate reservoir to evolve away from that of the global ocean. However, the Lower Aptian Gucuo II section derives from an open shallow sea on the northern margin of the Indian continent (Fig. 1C), directly facing the open Neo-Tethys Ocean. There is additional evidence for well-mixed watermass between the study area and the global ocean: (i) the Lower Aptian ammonites and foraminiferal species identified in Gucuo II have close affinity with those from other globally distributed marine sites (Hu *et al.*, 2008; Chen *et al.*, 2017); and (ii) the profile and absolute values of $\delta^{13}C_{org}$ from Gucuo II are closely comparable to those from other sites globally (Chen *et al.*, 2017). These observations suggest that a low seawater sulphate concentration before and during OAE 1a was likely to have been at least a (supra) regional, or even a global phenomenon. This conclusion is supported by previous studies of fluid-inclusion data of 5 to 12 mM (*ca* 124 to 122 Ma; Lowenstein *et al.*, 2003), and sulphur-cycle modelling results of less than 7 mM (Gomes *et al.*, 2016) and even lower than 0.6 mM (Bauer *et al.*, 2022a). The greatly reduced seawater $[SO_4^{2-}]$ could have resulted from large-scale episodic precipitation of gypsum in the proto-South Atlantic, both before (Wortmann & Chernyavsky, 2007) and during OAE 1a (Tedeschi *et al.*, 2017).

Implications for oceanic anoxic events

With respect to Mesozoic OAEs, the occurrence of siderite as evidence for a low-sulphate ocean has hitherto been reported for the Early Jurassic T-OAE (Xu *et al.*, 2018) and Early Cretaceous OAE 1a (Bauer *et al.*, 2022a). This interpretation is supported by the sulphur-isotope modelling results of 0.6 to 5.0 mM for the Early Toarcian (Gill *et al.*, 2011; Newton *et al.*, 2011; Han *et al.*, 2022), and 0.6 mM or even as low as 0.1 mM during OAE 1a (Bauer *et al.*, 2022a), as mentioned above. In addition to precipitation of evaporites before and during the OAEs, coupled elevated organic-carbon and associated pyrite burial during the OAEs could also have driven the sulphate concentrations to lower values (Jenkyns, 2010; Tedeschi *et al.*, 2017; Turner & Pelz, 2017). Although siderite has been only reported from sediments deposited during the T-OAE (Xu *et al.*, 2018) and OAE 1a (Bauer *et al.*, 2022a; this study), the current geochemical data from other typical Mesozoic OAE intervals suggest that marine low-sulphate concentrations were pervasive before and during OAEs. To date, sulphur-isotope modelling results and/or fluid-inclusion data from evaporites have confirmed that seawater $[SO_4^{2-}]$ was possibly less than 1 mM during the PTB (Luo *et al.*, 2010), less than 1 mM before the TJB (He *et al.*, 2020), *ca* 1.4 to 3.0 mM before OAE 2 (Adams *et al.*, 2010), and *ca* 2.1 to 7 mM during OAE 2 (Adams *et al.*, 2010; Owens *et al.*, 2013; Gomes *et al.*, 2016). These estimated sulphate concentrations are four to 50 times lower than that of the modern ocean (*ca* 29 mM).

The observations above support a probable cause and effect relationship between low seawater $[SO_4^{2-}]$ and widespread development of OAEs by the way of microbially mediating biogeochemical pathways (especially the ultimate limiting nutrient cycle of phosphorus and the movement of a sulphate–methane transition zone in the sediment pile) in the Mesozoic greenhouse world (Gomes *et al.*, 2016; He *et al.*, 2020; Bauer *et al.*, 2022b; and references therein). As discussed above, redox proxies record sediment deposition dominantly beneath suboxic (ferruginous) waters during the Early Aptian in the Tethys Himalaya. Previous studies suggested that ferruginous conditions could have resulted in elevated phosphorus burial and sequestration in sediments by adsorption to Fe minerals and/organic matter, in contrast to effective phosphorus recycling under sulphidic conditions (März *et al.*, 2008; Bauer *et al.*, 2022b). However, Poulton *et al.* (2015) suggested that either preferential release of phosphorus from organic matter or sulphide-promoted reduction of Fe oxides during MSR were sufficient to remobilize the sequestered phosphorus back into seawater. Therefore, it is hypothesized that,

under the precondition of low seawater [SO_4^{2-}], LIP activity and enhanced continental and marine basalt–seawater interaction could have elevated the sulphate input and thus the seawater [SO_4^{2-}], which greatly facilitated release of phosphorus and consequently led to subsequent enhanced primary productivity (cf. Adams *et al.*, 2010; Gomes *et al.*, 2016). Additionally, low seawater [SO_4^{2-}] could have led to a narrow sulphate–methane transition zone, moving it closer to the sediment–water interface (SWI) (i.e. producing a smaller sulphate reduction zone), thereby reducing the consumption of organic matter by MSR (e.g. He *et al.*, 2020). A higher organic-carbon flux thus could have been used by methanogens to produce methane that, however, could not be significantly removed in the sulphate reduction zone by anaerobic oxidation, but rather consumed by aerobic oxidation followed by upward diffusion to the seafloor, thus aggravating submarine anoxia (Whiticar, 1999; Knittel & Boetius, 2009; He *et al.*, 2020). Because of limited sulphate and oxygen availability in the sediment pile during OAEs, the methane would tend to accumulate in the ocean and then be released to the atmosphere (He *et al.*, 2020). Such a phenomenon would have resulted in an increased concentration of a potent greenhouse gas (methane), which could have significantly further reduced the dissolved oxygen in seawater and enhanced global warming.

The hypothesis of enhanced phosphorus availability via release from organic-matter remineralization and iron oxyhydr(oxide) dissolution has only been suggested in the case of OAE 1a and OAE 2 (Adams *et al.*, 2010; Poulton *et al.*, 2015; Gomes *et al.*, 2016). By contrast, the increase in benthic methane flux and associated expanded anoxia have been widely applied in the case of the highly inimical conditions reconstructed for the end-Permian mass extinction (Luo *et al.*, 2010) and Triassic–Jurassic boundary event (He *et al.*, 2020), as well as the Early Aptian OAE 1a (Bauer *et al.*, 2022a). The data presented in this study support the phosphorus-limiting hypothesis based on the fact that the obvious increase in pyrite occurrence is broadly synchronous with the eruption age of the Ontong Java LIP (Fig. 2), which likely supplied sulphate to marine waters, promoted MSR and organic-matter mineralization and released phosphorus.

The current data show that formation of siderite was pervasive in suboxic (ferruginous) environments before and during OAE 1a, just as in the case of the T-OAE (Xu *et al.*, 2018). These observations suggest that, under these sulphate-limited conditions, inorganic carbon burial associated with the formation of siderite may have also played a significant role in removing the isotopically light carbon injected into the ocean–atmosphere system from LIP activity and/or other sources. This hypothesis is supported by the fact that, during typical OAEs, enhanced continental weathering and basalt–seawater interaction was able to supply sufficient iron for the DIR process to produce enough reduced Fe^{2+} and HCO_3^-, probably accompanied by HCO_3^- from the methanogenic zone, to form the $FeCO_3$.

CONCLUSIONS

This study presents an integrated petrographic, mineralogical and geochemical study of siderite and pyrite hosted in dark grey shale and associated concretions of Early Aptian age in the Gucuo II section from the Tibetan Himalaya. The section derives from an open-marine setting on the northern margin of India in the Southern Hemisphere. The redox-sensitive elements, middle rare earth element (MREE) bulge pattern and relatively high total organic carbon (TOC) content suggest a dominantly suboxic (ferruginous) environment. Siderite occurs throughout the section in both dark grey shale and concretions and can be classified into three categories: disseminated (<5 μm), rhombic (*ca* 5 to 20 μm) and spherical (*ca* 0.1 to 1 μm) according to the morphological characteristics. The recognition of early diagenetic siderite in the dark grey shales, relatively low carbon-isotope ratios (with values close to that of organic matter) in the sideritic concretions, MREE bulge patterns from concretions and dark grey shales, as well as associated minor pyrite, indicate that relevant formational processes occurred in the iron reduction zone with particular conditions of low [SO_4^{2-}], reducing environment and abundant iron, and were thus significantly mediated by dissimilatory iron reduction (DIR). Two intervals of relatively elevated pyrite occurrence developed before and during oceanic anoxic event 1a (OAE 1a) interval, suggesting transient increase of sulphate concentrations, one episode of which corresponded to the onset of the OAE 1a negative $\delta^{13}C$ excursion, and can be ascribed to the input of sulphate from the emplacement of the Ontong Java large igneous province (LIP). The coexistence of siderite and pyrite may indicate that DIR occurred close to the microbial sulphate

reduction (MSR) zone, and the extremely low seawater [SO_4^{2-}] hovered around the threshold where pyrite could form once the seawater sulphate concentrations had increased due to episodic influx of fluids from enhanced continental and marine weathering and/or hydrothermal activity and/or volcanism. Observations support the previous hypothesis that, under a background of low [SO_4^{2-}], enhanced volcanic-derived sulphate input could have promoted MSR and organic-matter mineralization, which further enhanced phosphorus recycling, thereby increasing primary productivity and organic-carbon burial, leading to more oxygen consumption and driving an expansion of oxygen minimum zones, as characterized many OAEs.

ACKNOWLEDGEMENTS

We are grateful to Jiawei He and Tao Deng for their help in field sampling, Lan Mu for her kind help in analysing major and trace elements, and Xianguo Lang for helpful discussion. This work was supported by the National Natural Science Foundation of China (Nos. 42272116, 42488201 and 42002121) and a research grant (2021-LAMD-K03) from the State Key Laboratory of Mineral Deposit Research of Nanjing University. This manuscript is a contribution to the IGCP 739. We thank editor Ying Zhou and three anonymous reviewers for their insightful comments which greatly improved the quality of the manuscript.

DATA AVAILABILITY STATEMENT

Data openly available in a public repository.

REFERENCES

Adams, D.D., **Hurtgen, M.T.** and **Sageman, B.B.** (2010) Volcanic triggering of a biogeochemical cascade during Oceanic Anoxic Event 2. *Nat. Geosci.*, **3**, 201–204.

Algeo, T.J., **Luo, G.M.**, **Song, H.Y.**, **Lyons, T.W.** and **Canfield, D.E.** (2015) Reconstruction of secular variation in seawater sulfate concentrations. *Biogeosciences*, **12**, 2131–2151.

Anderson, T.F. and **Raiswell, R.** (2004) Sources and mechanisms for the enrichment of highly reactive iron in euxinic Black Sea sediments. *Am. J. Sci.*, **304**, 203–233.

Barling, J. and **Anbar, A.D.** (2004) Molybdenum isotope fractionation during adsorption by manganese oxides. *Earth Planet. Sci. Lett.*, **217**, 315–329.

Bauer, K.W., **Bottini, C.**, **Frei, R.**, **Asael, D.**, **Planavsky, N.J.**, **Francois, R.**, **McKenzie, N.R.**, **Erba, E.** and **Crowe, S.A.** (2021) Pulsed volcanism and rapid oceanic deoxygenation during Oceanic Anoxic Event 1a. *Geology*, **49**, 1452–1456.

Bauer, K.W., **Bottini, C.**, **Katsev, S.**, **Jellinek, M.**, **Francois, R.**, **Erba, E.** and **Crowe, S.A.** (2022a) Ferruginous oceans during OAE1a and collapse of the marine sulfate pool. *Earth Planet. Sci. Lett.*, **578**, 117324.

Bauer, K.W., **McKenzie, N.R.**, **Bottini, C.**, **Erba, E.** and **Crowe, S.A.** (2022b) Carbon pump dynamics and limited organic carbon burial during OAE1a. *Geobiology*, **21**, 341–354.

Bekker, A., **Slack, J.F.**, **Planavsky, N.**, **Krapež, B.**, **Hofmann, A.**, **Konhauser, K.O.** and **Rouxel, O.J.** (2010) Iron formation: the sedimentary product of a complex interplay among Mantle, Tectonic, Oceanic, and Biospheric Processes*. *Econ. Geol.*, **105**, 467–508.

Berner, R.A. (1981) A new geochemical classification of sedimentary environments. *J. Sediment. Res.*, **51**, 359–365.

Bodin, S., **Godet, A.**, **Westermann, S.** and **Föllmi, K.B.** (2013) Secular change in northwestern Tethyan water-mass oxygenation during the late Hauterivian–early Aptian. *Earth Planet. Sci. Lett.*, **374**, 121–131.

Bond, D.P.G. and **Wignall, P.B.** (2010) Pyrite framboid study of marine Permian–Triassic boundary sections: a complex anoxic event and its relationship to contemporaneous mass extinction. *GSA Bull.*, **122**, 1265–1279.

Bottini, C., **Cohen, A.S.**, **Erba, E.**, **Jenkyns, H.C.** and **Coe, A.L.** (2012) Osmium-isotope evidence for volcanism, weathering, and ocean mixing during the early Aptian OAE 1a. *Geology*, **40**, 583–586.

Canfield, D.E. and **Thamdrup, B.** (2009) Towards a consistent classification scheme for geochemical environments, or, why we wish the term 'suboxic' would go away. *Geobiology*, **7**, 385–392.

Chen, X., **Idakieva, V.**, **Stoykova, K.**, **Liang, H.**, **Yao, H.** and **Wang, C.** (2017) Ammonite biostratigraphy and organic carbon isotope chemostratigraphy of the early Aptian oceanic anoxic event (OAE 1a) in the Tethyan Himalaya of southern Tibet. *Palaeogeogr. Palaeoclimatol. Palaeoecol.*, **485**, 531–542.

Clapham, M.E. and **Renne, P.R.** (2019) Flood basalts and mass extinctions. *Annu. Rev. Earth Planet. Sci.*, **47**, 275–303.

Curtis, C.D. and **Spears, D.A.** (1968) The formation of sedimentary iron minerals. *Econ. Geol.*, **63**, 257–270.

Davidson, P.C., **Koppers, A.A.P.**, **Sano, T.** and **Hanyu, T.** (2023) A younger and protracted emplacement of the Ontong Java Plateau. *Science*, **380**, 1185–1188.

Erba, E., **Bottini, C.**, **Weissert, H.J.** and **Keller, C.E.** (2010) Calcareous nannoplankton response to surface-water acidification around Oceanic Anoxic Event 1a. *Science*, **329**, 428–432.

Erba, E., **Duncan, R.A.**, **Bottini, C.**, **Tiraboschi, D.**, **Weissert, H.**, **Jenkyns, H.C.** and **Malinverno, A.** (2015) Environmental consequences of Ontong Java Plateau and Kerguelen plateau volcanism. In: *The Origin, Evolution, and Environmental Consequences of Oceanic Large Igneous Provinces* (Eds Neal, C.R., Sager, W.W., Sano, T. and Erba, E.), *Geol. Soc. Am. Spec. Paper*, **511**, 271–303. Geological Society of America, Boulder, CO.

Fairbridge, R.W. (1967) Chapter 2 Phases of diagenesis and authigenesis. In: *Developments in Sedimentology* (Eds Larsen, G. and Chilingar, G.V.), Vol. **8**, pp. 19–89. Elsevier, Amsterdam.

Fike, D.A., **Bradley, A.S.** and **Rose, C.V.** (2015) Rethinking the ancient sulfur cycle. *Annu. Rev. Earth Planet. Sci.*, **43**, 593–622.

Foster, G.L., **Hull, P.**, **Lunt, D.J.** and **Zachos, J.C.** (2018) Placing our current 'hyperthermal' in the context of rapid climate change in our geological past. *Philos. Trans. R. Soc. A*, **376**, 20170086.

Gaines, R.R. and **Vorhies, J.S.** (2016) Growth mechanisms and geochemistry of carbonate concretions from the Cambrian Wheeler Formation (Utah, USA). *Sedimentology*, **63**, 662–698.

Gansser, A. (1964) *Geology of the Himalayas*. Interscience Publishers John Wiley and Sons, New York. (289 pp.).

Garcia, T.I., **Gorton, M.P.**, **Li, H.**, **Wortmann, U.G.** and **Spooner, E.T.C.** (2016) The geochemistry of the 2.75 Ga-old Helen Iron Formation, Wawa, Ontario – Insights into iron formation deposition from carbon isotopes and rare earth elements. *Precambrian Res.*, **275**, 357–368.

German, C.R. and **Elderfield, H.** (1989) Rare earth elements in Saanich Inlet, British Columbia, a seasonally anoxic basin. *Geochim. Cosmochim. Acta*, **53**, 2561–2571.

Gill, B.C., **Lyons, T.W.** and **Jenkyns, H.C.** (2011) A global perturbation to the sulfur cycle during the Toarcian Oceanic Anoxic Event. *Earth Planet. Sci. Lett.*, **312**, 484–496.

Gomes, M.L., **Hurtgen, M.T.** and **Sageman, B.B.** (2016) Biogeochemical sulfur cycling during Cretaceous oceanic anoxic events: A comparison of OAE1a and OAE2. *Paleoceanography*, **31**, 233–251.

Halama, M., **Swanner, E.D.**, **Konhauser, K.O.** and **Kappler, A.** (2016) Evaluation of siderite and magnetite formation in BIFs by pressure–temperature experiments of Fe(III) minerals and microbial biomass. *Earth Planet. Sci. Lett.*, **450**, 243–253.

Haley, B.A., **Klinkhammer, G.P.** and **McManus, J.** (2004) Rare earth elements in pore waters of marine sediments. *Geochim. Cosmochim. Acta*, **68**, 1265–1279.

Han, Z., **Hu, X.**, **Li, J.** and **Garzanti, E.** (2016) Jurassic carbonate microfacies and relative sea-level changes in the Tethys Himalaya (southern Tibet). *Palaeogeogr. Palaeoclimatol. Palaeoecol.*, **456**, 1–20.

Han, Z., **Hu, X.**, **Hu, Z.**, **Jenkyns, H.C.** and **Su, T.** (2022) Geochemical evidence from the Kioto Carbonate Platform (Tibet) reveals enhanced terrigenous input and deoxygenation during the early Toarcian. *Glob. Planet. Chang.*, **215**, 103887.

He, T., **Dal Corso, J.**, **Newton, R.J.**, **Wignall, P.B.**, **Mills, B.J.W.**, **Todaro, S.**, **Di Stefano, P.**, **Turner, E.C.**, **Jamieson, R.A.**, **Randazzo, V.**, **Rigo, M.**, **Jones, R.E.** and **Dunhill, A.M.** (2020) An enormous sulfur isotope excursion indicates marine anoxia during the end-Triassic mass extinction. *Sci. Adv.*, **6**, eabb6704.

Heimann, A., **Johnson, C.M.**, **Beard, B.L.**, **Valley, J.W.**, **Roden, E.E.**, **Spicuzza, M.J.** and **Beukes, N.J.** (2010) Fe, C, and O isotope compositions of banded iron formation carbonates demonstrate a major role for dissimilatory iron reduction in ~2.5Ga marine environments. *Earth Planet. Sci. Lett.*, **294**, 8–18.

Helz, G.R., **Bura-Nakić, E.**, **Mikac, N.** and **Ciglenečki, I.** (2011) New model for molybdenum behavior in euxinic waters. *Chem. Geol.*, **284**, 323–332.

Hu, X., **Jansa, L.** and **Wang, C.** (2008) Upper Jurassic–Lower Cretaceous stratigraphy in south-eastern Tibet: a comparison with the western Himalayas. *Cretac. Res.*, **29**, 301–315.

Hu, X., **Li, J.**, **Han, Z.** and **Li, Y.** (2020) Two types of hyperthermal events in the Mesozoic-Cenozoic: Environmental impacts, biotic effects, and driving mechanisms. *Sci. China Earth Sci.*, **63**, 1041–1058.

Huang, L. (2004) On siderite in Tongziyan Formation, Longyong Coalifield and Its Lithofacies Meaning. *Coal Geol. China*, **16**, 35–37 (in Chinese).

Irwin, H., **Curtis, C.** and **Coleman, M.** (1977) Isotopic evidence for source of diagenetic carbonates formed during burial of organic-rich sediments. *Nature*, **269**, 209–213.

Jadoul, F., **Berra, F.** and **Garzanti, E.** (1998) The Tethys Himalayan passive margin from Late Triassic to Early Cretaceous (South Tibet). *J. Asian Earth Sci.*, **16**, 173–194.

Jenkyns, H.C. (2003) Evidence for rapid climate change in the Mesozoic–Palaeogene greenhouse world. *Philos. Trans. R. Soc. A*, **361**, 1885–1916.

Jenkyns, H.C. (2010) Geochemistry of oceanic anoxic events. *Geochem. Geophys. Geosyst.*, **11**, Q03004.

Jenkyns, H.C. (2018) Transient cooling episodes during Cretaceous Oceanic Anoxic Events with special reference to OAE 1a (Early Aptian). *Philos. Trans. R. Soc. A*, **376**, 20170073.

Jones, B. and **Manning, D.A.C.** (1994) Comparison of geochemical indices used for the interpretation of palaeoredox conditions in ancient mudstones. *Chem. Geol.*, **111**, 111–129.

Kaźmierczak, J. (1979) The eukaryotic nature of Eosphaera-like ferriferous structures from the Precambrian Gunflint Iron Formation, Canada: a comparative study. *Precambrian Res.*, **9**, 1–22.

Keller, C.E., **Hochuli, P.A.**, **Weissert, H.**, **Bernasconi, S.M.**, **Giorgioni, M.** and **Garcia, T.I.** (2011) A volcanically induced climate warming and floral change preceded the onset of OAE1a (Early Cretaceous). *Palaeogeogr. Palaeoclimatol. Palaeoecol.*, **305**, 43–49.

Knittel, K. and **Boetius, A.** (2009) Anaerobic oxidation of methane: progress with an unknown process. *Ann. Rev. Microbiol.*, **63**, 311–334.

Köhler, I., **Konhauser, K.O.**, **Papineau, D.**, **Bekker, A.** and **Kappler, A.** (2013) Biological carbon precursor to diagenetic siderite with spherical structures in iron formations. *Nat. Commun.*, **4**, 1741.

Konhauser, K.O., **Newman, D.K.** and **Kappler, A.** (2005) The potential significance of microbial Fe(III) reduction during deposition of Precambrian banded iron formations. *Geobiology*, **3**, 167–177.

Krylov, A., **Khlystov, O.**, **Zemskaya, T.**, **Minami, H.**, **Hachikubo, A.**, **Nunokawa, Y.**, **Kida, M.**, **Shoji, H.**, **Naudts, L.**, **Poort, J.** and **Pogodaeva, T.** (2008) First discovery and formation process of authigenic siderite from gas hydrate–bearing mud volcanoes in fresh water: Lake Baikal, Eastern Siberia. *Geophys. Res. Lett.*, **35**, LO5405.

Kump, L.R. and **Arthur, M.A.** (1999) Interpreting carbon-isotope excursions: carbonates and organic matter. *Chem. Geol.*, **161**, 181–198.

LaBerge, G.L. (1973) Possible biological origin of precambrian iron-formations. *Econ. Geol.*, **68**, 1098–1109.

Lawrence, M.G., **Greig, A.**, **Collerson, K.D.** and **Kamber, B.S.** (2006) Rare earth element and yttrium variability in south east Queensland waterways. *Aquat. Geochem.*, **12**, 39–72.

Liang, H., **Chen, X.**, **Wang, C.**, **Zhao, D.** and **Weissert, H.** (2016) Methane-derived authigenic carbonates of mid-Cretaceous age in southern Tibet: Types of carbonate

concretions, carbon sources, and formation processes. *J. Asian Earth Sci.*, **115**, 153–169.

Liu, G. and **Einsele, G.** (1994) Sedimentary history of the Tethyan basin in the Tibetan Himalayas. *Geol. Rundsch.*, **83**, 32–61.

Liu, A.-Q., **Tang, D.-J.**, **Shi, X.-Y.**, **Zhou, L.-M.**, **Zhou, X.-Q.**, **Shang, M.-H.**, **Li, Y.** and **Song, H.-Y.** (2019) Growth mechanisms and environmental implications of carbonate concretions from the ~1.4 Ga Xiamaling Formation, North China. *J. Palaeogeogr.*, **8**, 20.

Lovley, D.R. (1991) Dissimilatory Fe(III) and Mn(IV) reduction. *Microbiol. Rev.*, **55**, 259–287.

Lowenstein, T.K., **Hardie, L.A.**, **Timofeeff, M.N.** and **Demicco, R.V.** (2003) Secular variation in seawater chemistry and the origin of calcium chloride basinal brines. *Geology*, **31**, 857–860.

Loyd, S.J., **Marenco, P.J.**, **Hagadorn, J.W.**, **Lyons, T.W.**, **Kaufman, A.J.**, **Sour-Tovar, F.** and **Corsetti, F.A.** (2012) Sustained low marine sulfate concentrations from the Neoproterozoic to the Cambrian: insights from carbonates of northwestern Mexico and eastern California. *Earth Planet. Sci. Lett.*, **339-340**, 79–94.

Luo, G., **Kump, L.R.**, **Wang, Y.**, **Tong, J.**, **Arthur, M.A.**, **Yang, H.**, **Huang, J.**, **Yin, H.** and **Xie, S.** (2010) Isotopic evidence for an anomalously low oceanic sulfate concentration following end-Permian mass extinction. *Earth Planet. Sci. Lett.*, **300**, 101–111.

Lyons, T.W. and **Severmann, S.** (2006) A critical look at iron paleoredox proxies: new insights from modern euxinic marine basins. *Geochim. Cosmochim. Acta*, **70**, 5698–5722.

März, C., **Poulton, S.W.**, **Beckmann, B.**, **Küster, K.**, **Wagner, T.** and **Kasten, S.** (2008) Redox sensitivity of P cycling during marine black shale formation: dynamics of sulfidic and anoxic, non-sulfidic bottom waters. *Geochim. Cosmochim. Acta*, **72**, 3703–3717.

McLennan, S.M. (1989) Rare earth elements in sedimentary rocks: influence of provenance and sedimentary processes. In: *Geochemistry and Mineralogy of Rare Earth Elements*, pp. 169–200. Mineralogic Society of America, Washington, D.C.

Menegatti, A.P., **Weissert, H.**, **Brown, R.S.**, **Tyson, R.V.**, **Farrimond, P.**, **Strasser, A.** and **Caron, M.** (1998) High-resolution δ13C stratigraphy through the Early Aptian "Livello selli" of the Alpine tethys. *Paleoceanography*, **13**, 530–545.

Mills, J.V., **Gomes, M.L.**, **Kristall, B.**, **Sageman, B.B.**, **Jacobson, A.D.** and **Hurtgen, M.T.** (2017) Massive volcanism, evaporite deposition, and the chemical evolution of the Early Cretaceous ocean. *Geology*, **45**, 475–478.

Morford, J.L., **Russell, A.D.** and **Emerson, S.** (2001) Trace metal evidence for changes in the redox environment associated with the transition from terrigenous clay to diatomaceous sediment, Saanich Inlet, BC. *Mar. Geol.*, **174**, 355–369.

Mozley, P.S. and **Burns, S.J.** (1993) Oxygen and carbon isotopic composition of marine carbonate concretions; an overview. *J. Sediment. Res.*, **63**, 73–83.

Mozley, P.S. and **Wersin, P.** (1992) Isotopic composition of siderite as an indicator of depositional environment. *Geology*, **20**, 817–820.

Newton, R.J., **Reeves, E.P.**, **Kafousia, N.**, **Wignall, P.B.**, **Bottrell, S.H.** and **Sha, J.-G.** (2011) Low marine sulfate concentrations and the isolation of the European epicontinental sea during the Early Jurassic. *Geology*, **39**, 7–10.

Nie, Y., **Fu, X.**, **Wei, H.**, **Lin, F.**, **Zeng, S.**, **Mansour, A.**, **Zhou, G.** and **Wang, W.** (2023) Paleoenvironmental reconstruction preceding and during the early Aptian Oceanic Anoxic Event 1a in southern Tibet, eastern Tethys. *Cretac. Res.*, **150**, 105604.

Ohkouchi, N., **Kawamura, K.**, **Kajiwara, Y.**, **Wada, E.**, **Okada, M.**, **Kanamatsu, T.** and **Taira, A.** (1999) Sulfur isotope records around Livello Bonarelli (northern Apennines, Italy) black shale at the Cenomanian–Turonian boundary. *Geology*, **27**, 535–538.

Ohmoto, H., **Watanabe, Y.** and **Kumazawa, K.** (2004) Evidence from massive siderite beds for a CO_2-rich atmosphere before, 1.8 billion years ago. *Nature*, **429**, 395–399.

Owens, J.D., **Gill, B.C.**, **Jenkyns, H.C.**, **Bates, S.M.**, **Severmann, S.**, **Kuypers, M.M.M.**, **Woodfine, R.G.** and **Lyons, T.W.** (2013) Sulfur isotopes track the global extent and dynamics of euxinia during Cretaceous Oceanic Anoxic Event 2. *Proc. Natl. Acad. Sci. USA*, **110**, 18407–18412.

Percival, L.M.E., **Tedeschi, L.R.**, **Creaser, R.A.**, **Bottini, C.**, **Erba, E.**, **Giraud, F.**, **Svensen, H.**, **Savian, J.**, **Trindade, R.**, **Coccioni, R.**, **Frontalini, F.**, **Jovane, L.**, **Mather, T.A.** and **Jenkyns, H.C.** (2021) Determining the style and provenance of magmatic activity during the Early Aptian Oceanic Anoxic Event (OAE 1a). *Glob. Planet. Chang.*, **200**, 103461.

Petrash, D.A., **Bialik, O.M.**, **Bontognali, T.R.R.**, **Vasconcelos, C.**, **Roberts, J.A.**, **McKenzie, J.A.** and **Konhauser, K.O.** (2017) Microbially catalyzed dolomite formation: from near-surface to burial. *Earth Sci. Rev.*, **171**, 558–582.

Poulson, R.L., **Siebert, C.**, **McManus, J.** and **Berelson, W.M.** (2006) Authigenic molybdenum isotope signatures in marine sediments. *Geology*, **34**, 617–620.

Poulton, S.W. and **Canfield, D.E.** (2011) Ferruginous conditions: a dominant feature of the ocean through earth's history. *Elements*, **7**, 107–112.

Poulton, S.W., **Henkel, S.**, **März, C.**, **Urquhart, H.**, **Flögel, S.**, **Kasten, S.**, **Sinninghe Damsté, J.S.** and **Wagner, T.** (2015) A continental-weathering control on orbitally driven redox-nutrient cycling during Cretaceous Oceanic Anoxic Event 2. *Geology*, **43**, 963–966.

Raiswell, R. (1987) Non-steady state microbiological diagenesis and the origin of concretions and nodular limestones. *Geol. Soc. Lond.*, **36**, 41–54.

Raiswell, R. and **Canfield, D.E.** (2012) The iron biogeochemical cycle past and present. *Geochem. Perspect*, **1**, 1–2.

Raiswell, R. and **Fisher, Q.J.** (2000) Mudrock-hosted carbonate concretions: a review of growth mechanisms and their influence on chemical and isotopic composition. *J. Geol. Soc. Lond.*, **157**, 239–251.

Raiswell, R. and **Fisher, Q.J.** (2004) Rates of carbonate cementation associated with sulphate reduction in DSDP/ODP sediments: implications for the formation of concretions. *Chem. Geol.*, **211**, 71–85.

Reershemius, T. and **Planavsky, N.J.** (2021) What controls the duration and intensity of ocean anoxic events in the Paleozoic and the Mesozoic? *Earth Sci. Rev.*, **221**, 103787.

Romanek, C.S., **Jiménez-López, C.**, **Navarro, A.R.**, **Sánchez-Román, M.**, **Sahai, N.** and **Coleman, M.** (2009) Inorganic synthesis of Fe–Ca–Mg carbonates at low temperature. *Geochim. Cosmochim. Acta*, **73**, 5361–5376.

Scotese, C.P. and **Golanka, J.** (1997) Paleogeographic Atlas, PALEOMAP progress report 20. University of Texas, 34.

Scott, C. and **Lyons, T.W.** (2012) Contrasting molybdenum cycling and isotopic properties in euxinic versus non-euxinic sediments and sedimentary rocks: refining the paleoproxies. *Chem. Geol.*, **324–325**, 19–27.

Sellés-Martínez, J. (1996) Concretion morphology, classification and genesis. *Earth Sci. Rev.*, **41**, 177–210.

Socorro, J., **Maurrasse, F.J.M.R.** and **Sanchez-Hernandez, Y.** (2017) Characterization of the negative carbon isotope shift in segment C2, its global implications as a harbinger of OAE1a. *Sci. China-Earth Sci.*, **60**, 30–43.

Tang, D., **Shi, X.**, **Jiang, G.**, **Wu, T.**, **Ma, J.** and **Zhou, X.** (2018) Stratiform siderites from the Mesoproterozoic Xiamaling Formation in North China: genesis and environmental implications. *Gondwana Res.*, **58**, 1–15.

Tedeschi, L.R., **Jenkyns, H.C.**, **Robinson, S.A.**, **Sanjinés, A.E.S.**, **Viviers, M.C.**, **Quintaes, C.M.S.P.** and **Vazquez, J.C.** (2017) New age constraints on Aptian evaporites and carbonates from the South Atlantic: implications for Oceanic Anoxic Event 1a. *Geology*, **45**, 543–546.

Teixeira, N.L., **Caxito, F.A.**, **Rosière, C.A.**, **Pecoits, E.**, **Vieira, L.**, **Frei, R.**, **Sial, A.N.** and **Poitrasson, F.** (2017) Trace elements and isotope geochemistry (C, O, Fe, Cr) of the Cauê iron formation, Quadrilátero Ferrífero, Brazil: evidence for widespread microbial dissimilatory iron reduction at the Archean/Paleoproterozoic transition. *Precambrian Res.*, **298**, 39–55.

Tejada, M.L.G., **Suzuki, K.**, **Kuroda, J.**, **Coccioni, R.**, **Mahoney, J.J.**, **Ohkouchi, N.**, **Sakamoto, T.** and **Tatsumi, Y.** (2009) Ontong Java Plateau eruption as a trigger for the early Aptian oceanic anoxic event. *Geology*, **37**, 855–858.

Timm, C., **Hoernle, K.**, **Werner, R.**, **Hauff, F.**, **van den Bogaard, P.**, **Michael, P.**, **Coffin, M.F.** and **Koppers, A.** (2011) Age and geochemistry of the oceanic Manihiki Plateau, SW Pacific: new evidence for a plume origin. *Earth Planet. Sci. Lett.*, **304**, 135–146.

Tostevin, R. (2021) *Cerium Anomalies and Paleoredox (Elements in Geochemical Tracers in Earth System Science)*. Cambridge University Press, Cambridge.

Tribovillard, N., **Algeo, T.J.**, **Lyons, T.** and **Riboulleau, A.** (2006) Trace metals as paleoredox and paleoproductivity proxies: an update. *Chem. Geol.*, **232**, 12–32.

Tribovillard, N., **Algeo, T.J.**, **Baudin, F.** and **Riboulleau, A.** (2012) Analysis of marine environmental conditions based onmolybdenum–uranium covariation—applications to Mesozoic paleoceanography. *Chem. Geol.*, **324-325**, 46–58.

Turner, P. and **Pelz, K.** (2017) Chapter 27 - Development of an Upper Triassic-Lower Jurassic Evaporite Basin on the Saharan Platform, North Africa. In: *Permo-Triassic Salt Provinces of Europe, North Africa and the Atlantic Margins* (Eds Soto, J.I., Flinch, J.F. and Tari, G.), pp. 581–599. Elsevier, Amsterdam.

Tyson, R.V. and **Pearson, T.H.** (1991) Modern and ancient continental shelf anoxia: an overview. *Geol. Soc. Lond.*, **58**, 1–24.

van der Weijden, C.H. (1992) Early diagenesis and marine pore water. In: *Developments in Sedimentology* (Eds Wolf, K.H. and Chilingarian, G.V.), Vol. **47**, pp. 13–134. Elsevier, Amsterdam.

Whiticar, M.J. (1999) Carbon and hydrogen isotope systematics of bacterial formation and oxidation of methane. *Chem. Geol.*, **161**, 291–314.

Wilkin, R.T., **Barnes, H.L.** and **Brantley, S.L.** (1996) The size distribution of framboidal pyrite in modern sediments: an indicator of redox conditions. *Geochim. Cosmochim. Acta*, **60**, 3897–3912.

Wortmann, U.G. and **Chernyavsky, B.M.** (2007) Effect of evaporite deposition on early cretaceous carbon and sulphur cycling. *Nature*, **446**, 654–656.

Xu, W., **Ruhl, M.**, **Jenkyns, H.C.**, **Leng, M.J.**, **Huggett, J.M.**, **Minisini, D.**, **Ullmann, C.V.**, **Riding, J.B.**, **Weijers, J.W.H.**, **Storm, M.S.**, **Percival, L.M.E.**, **Tosca, N.J.**, **Idiz, E.F.**, **Tegelaar, E.W.** and **Hesselbo, S.P.** (2018) Evolution of the Toarcian (Early Jurassic) carbon-cycle and global climatic controls on local sedimentary processes (Cardigan Bay Basin, UK). *Earth Planet. Sci. Lett.*, **484**, 396–411.

Manuscript received 5 March 2023; revision accepted 3 June 2024

Supporting Information

Additional information may be found in the online version of this article:

Table S1. Element compositions and atom ratios of siderites.

Table S2. Major and trace elements of dark grey shales.

Table S3. Rare-earth elements (REEs) of dark grey shales and concretions.